

# **Interfacial Electron Transfer Kinetics for Fully Vibrationally Characterized Systems: Insights from Complete Multi-mode Quantum Rate Calculations**

Donald C. Selmarten and Joseph T. Hupp  
Dept. of Chemistry  
Northwestern University  
2145 Sheridan Road  
Evanston, IL 60208

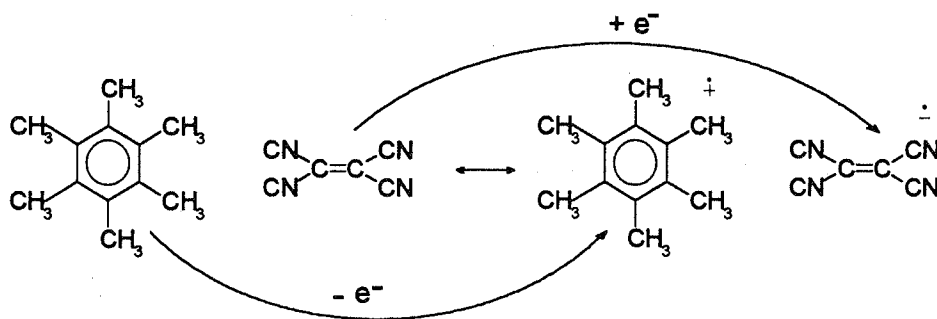
Nominally "simple" outer-sphere electron transfer reactions can be complex in a vibrational reorganizational sense. For reactants capable of forming Mulliken-type charge transfer complexes, resonance Raman intensity data can be utilized to obtain unitless normal coordinate displacements, mode-specific vibrational reorganizational parameters and multi-dimensional potential energy surfaces for the corresponding electrochemical half reactions. The displacement and reorganizational parameters, in turn, can be employed in a multi-mode quantum rate formulation to obtain complete mode-specific descriptions of vibrational rate attenuation effects, driving force effects, temperature effects and nuclear tunneling effects. The strategy is illustrated for the electrochemical reduction of tetracyanoethylene (4 vibrational modes) and the electrochemical oxidation of hexamethylbenzene (6 vibrational modes).

## **INTRODUCTION**

It is generally accepted that activation barriers to interfacial electron transfer are comprised of both solvational and vibrational reorganizational components. Over the past seven years it has become possible to assess mode or bond specific components of electron transfer barriers for chemically complex systems in unprecedented quantitative detail (1-9). The methodology is based on experimental resonance or preresonance (charge-transfer enhanced) Raman scattering together with a time-dependent overlap (wave packet propagation) analysis of scattering intensities and absorption or emission line shapes (10,11). Representative of redox systems successfully characterized by this approach are 4-cyano-N-methylpyridinium<sup>+0</sup> (4), ferrocenium/ferrocene (biferrocene monocation) (5), nitrobenzene<sup>+0</sup> tethered to a cadmium sulfide cluster (6), ferri-/ferrocyanide on titanium dioxide (7) and several intramolecular charge transfer systems (3,8,9). The availability of such detailed vibrational barrier information makes possible, in principle, the assessment of *all* vibrational factors that affect or control a given interfacial electron transfer rate.

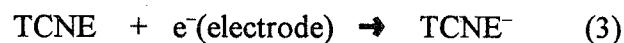
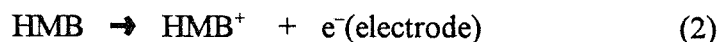
In this paper we describe the results of complete multi mode (i.e. many dimensional)

rate calculations for a representative pair of redox couples: hexamethylbenzene<sup>+0</sup> (HMB<sup>+0</sup>) and tetracyanoethylene<sup>0/-</sup> (TCNE<sup>0/-</sup>). The approach taken is to recognize the coupled half-reaction nature of donor/acceptor transitions in Mulliken charge transfer complexes, including the 1:1 complex formed by HMB and TCNE:



(1)

We then make use of recently published time-dependent analyses of absorption, emission and scattering effects associated with reaction 1 (1,2) to obtain mode-specific vibrational displacements and reorganizational barrier contributions for electrochemical reactions 2 and 3:



Finally, we combine the vibrational information with calculated solvent barrier information and employ radiationless decay theory (12) to obtain fully quantum mechanical estimates of electron exchange rates, activation parameters and mode-specific rate attenuation and tunneling effects. The combined analysis provides unusually detailed – almost unprecedented – computational descriptions of interfacial reaction kinetics for representative neutral/radical-cation and neutral/radical-anion pairs.

## RESULTS AND DISCUSSION

*Coordinate displacements, reorganizational energies and ET reaction surfaces.* Myers and co-workers have used wavepacket propagation techniques to extract absolute values of unitless coordinate displacements ( $\Delta$ ) for reaction 1 from resonance Raman

scattering intensities and charge-transfer fluorescence line shapes (1,2). We refer the interested reader to refs. 1-11 for technical details, but note that (in principle) the methodology can be applied to any electron transfer reaction for which a corresponding optical charge transfer transition is observable. In any case, the displacements reported for reaction 1 are almost *but not quite* the displacements needed for reactions 2 and 3. The differences come from the less than complete degree of charge transfer achieved in eq. 1. Analysis of vibrational frequency differences for the isolated acceptor (TCNE) (13), reduced acceptor (TCNE<sup>-</sup>) (13) and the donor/acceptor pair (HMB/TCNE) (14) leads to the conclusion that approximately 7% of a unit electronic charge has already been transferred in the ground state or reactant donor/acceptor pair (l.h.s. eq. 1). If a similar degree of "back charge transfer" exists in the product pair (r.h.s. eq. 1), then a net transfer of 85% of a unit electronic charge occurs. The corresponding electrochemical reactions, on the other hand, necessarily involve transfer of an entire electron. Various empirical relationships suggest that coordinate displacements (for a given mode) scale linearly with both the extent of charge transfer and the magnitude of the reactant/product vibrational frequency difference (15-17). The desired electrochemical displacement parameters, therefore, can be obtained simply by rescaling the available optical parameters by 1/0.85. Tables 1 and 2 list the electrochemical displacement parameters.

It is important to note that displacements obtained in this way describe normal modes involving (usually) several atoms and several bonds. In principle, if a full normal coordinate analysis is available, the unitless normal coordinate displacements can be converted to local coordinate displacements (bond length changes) having units of distance. For subsequent rate calculations, however, the displacement parameters are most easily utilized by keeping them in unitless form. In this form, single-mode contributions to the vibrational reorganization energy are given by eq. 4:

$$\chi'_{\text{vib}} = 0.5\Delta^2\nu \quad (4)$$

where  $\nu$  is the vibrational frequency. Tables 1 and 2 list  $\chi'_{\text{vib}}$  values for all modes contributing to reactions 2 and 3.

Figure 1 illustrates the relationship between the *total* reorganization energy, the overpotential and the classical activation barrier for a generic interfacial electron transfer reaction (18). In this 2-dimensional diagram, the reaction coordinate represents an appropriately weighted average of displacements for all Franck-Condon active vibrational and solvational coordinates. Figure 2a shows a more informative 3-dimensional diagram – specifically for TCNE reduction – in which the reaction coordinate is now separated into a Raman-derived composite vibrational component and a solvational component. (The solvent reorganization energy,  $\chi_s$ , was calculated for acetonitrile as solvent by using Marcus theory (18). The reaction site was assumed to lie just beyond a chemisorbed solvent inner layer and the reactant was assumed to be coplanar with the electrode surface. The decidedly nonspherical reactants were represented as equivalent spheres (required by conventional Marcus theory) by taking the equivalent radius to be the cube root of the product of radii in the x, y and z directions. For TCNE<sup>0/-</sup>, this approach yields 42 kJ mol<sup>-1</sup> for  $\chi_s$ ; for HMB<sup>+0</sup>,

the calculated value for  $\chi_s$  is 36 kJ mol<sup>-1</sup>.)

Given the entries in Tables 1 and 2, the actual ET reaction surfaces clearly are more complicated than suggested by Figure 2a. Indeed, TCNE reduction proceeds on a 6-dimensional surface (4 vibrations + solvent + energy), while HMB oxidation occurs on an 8-dimensional surface (6 vibrations + solvent + energy). If harmonic potentials are assumed then the tables contain all of the information necessary to construct these surfaces. Of course, graphical representation of more than three dimensions is not feasible. In Figures 2b and 2c, however, we show representative three dimensional slices of the 6-dimensional TCNE<sup>0/-</sup> surfaces under zero driving force conditions. Note that in these figures, "reaction coordinates" (or more accurately, fragments of reaction coordinates) now have precise molecular meanings: They correspond exactly to Raman-derived unitless coordinate displacements. In addition, saddle points on these diagrams correspond precisely to classical activation barrier contributions for the pair of vibrations contained in each calculation.

*Single-mode classical and multi-mode quantum rate calculations.* If we assume nonadiabatic reaction kinetics, the classical rate constant for outer-sphere interfacial electron transfer at a fixed potential,  $E$ , can be written as:

$$k_{ET} = \delta d (4\pi^2 H_{12}^2 / h) (4\pi \chi_s RT)^{-1/2} \exp(-\Delta G^*(\text{class})/RT) \quad (4)$$

where

$$\Delta G^*(\text{class}) = [\pm(F/RT)(E_f - E) + \chi]^2 / 4\chi \quad (5)$$

In the equations,  $\delta d$  is an effective reaction zone thickness (taken as 0.6 Å) (19),  $H_{12}$  is the initial-state/final-state electronic coupling energy,  $h$  is Planck's constant,  $\Delta G^*(\text{class})$  is the classical activation free energy,  $E_f$  is the formal potential,  $E$  is the applied potential and  $R$ ,  $T$  and  $F$  have their usual meanings. For reduction (eq. 3), the sign in eq. 5 is positive; for oxidation (eq. 2) it is negative. For computational purposes we assumed that both reaction types were marginally nonadiabatic in a dynamical sense and that the longitudinal relaxation time of the solvent (20,21) was an appropriate dynamical benchmark. The pair of assumptions then yields  $4 \times 10^{12} \text{ s}^{-1}$  for the product of the two terms in parentheses in the pre-exponential portion of eq. 4.

Application of eqs. 4 and 5 to TCNE reduction and HMB oxidation, assuming that only solvent is reorganized, yields the rate constant versus electrochemical driving force plots shown in Figures 3 and 4 (dashed curves). Note that in both cases the rate initially increases with increasing overpotential, but ultimately decreases for high overpotentials. The rate decrease is a straightforward computational manifestation of the Marcus inverted region effect (18) and is experimentally observable for selected reactions at wide bandgap semiconductor electrodes (22). For reactions at metal electrodes, however, the existence of a continuum of filled electronic states below the Fermi level and a continuum of empty states above the Fermi level makes the actual rate a convolution of rates over all accessible

levels, with the fastest rates obviously making the largest contributions (18). The convolution effectively eliminates the rate inversion effect experimentally. To account for the convolution we have implemented a variant of Chidsey's "sum over electronic states" approach (23), as described elsewhere (4). For simplicity (and because we lack needed information regarding densities of electronic (electrode) states) we then normalized the sum-over-states results to the values of  $k_{\text{ET}}$  obtained from the conventional expression (eq. 4) at  $E = E_f$ . The resulting corrected curves are shown as solid lines in Figures 3 and 4.

To account for vibrational reorganizational effects we chose to discard the classical activation barrier approach and use a "golden rule" approach (12, 24). As illustrated in Figure 5, this approach emphasizes the key role of initial-state/final-state vibrational overlaps in defining reactivity. While the required overlaps clearly are greatest at the point where classical potential energy surfaces intersect, they also can attain finite values at points well below (and above) the intersection region. Particularly for high frequency modes, this can lead to enhanced reactivity that is sometimes described as finite nuclear tunneling. In any case, a simplified golden-rule-based rate expression is the following:

$$(6) \quad k_{\text{ET}} = \delta r (4\pi^2 H_{12}^2 / h) \rho_{\text{vib}}$$

where

$$\rho_{\text{vib}} = \sum_w | \langle X_{1v} | X_{2w} \rangle |^2 \delta (\epsilon_{1v} - \epsilon_{2w}) \quad (7)$$

In the equations,  $\rho_{\text{vib}}$  is a *vibrational* density of states term,  $X_{1v}$  is a wavefunction for vibrational state  $v$  of the initial electronic state,  $X_{2w}$  is a wavefunction for a manifold of vibrational states associated with the final electronic state,  $\epsilon_{1v}$  and  $\epsilon_{2w}$  are energies of specific vibrational levels and  $\delta$  is the Dirac delta function (where the purpose of the delta function is to ensure that energy is conserved during the ET reaction). A more explicit form of the vibrational density of states function is the following (24,25):

$$\begin{aligned}
\rho_{\text{vib}} = & \overbrace{(4\pi \chi_s kT)^{-1/2}}^{\text{a}} \exp \left[ -\overbrace{\left( \sum_j S_j \coth(h\nu_j/2kT) \right)}^{\text{b}} \right] \times \\
& \overbrace{\prod_j \sum_{m_j=-\infty}^{+\infty} \exp(m_j h\nu_j/kT) I_{|m_j|} \{ S_j \text{csch}(h\nu_j/2kT) \}}^{\text{c}} \times \\
& \exp \left[ -\overbrace{\frac{(\Delta E + \chi_s + \sum_j m_j h\nu_j)^2}{4\chi_s RT}}^{\text{d}} \right] \quad (8)
\end{aligned}$$

In eq. 8,  $S$  equals  $\Delta^2/2$ ,  $m$  is the change in vibrational quantum number accompanying the reaction,  $I_m$  is a modified Bessel function of order  $m$ , and  $\Delta E$  is the energy of the final state minus the initial state. After units conversion, the energy term can be equated with the overpotential for an electrochemical reduction or the negative of the overpotential for an electrochemical oxidation. Eq. 8 obviously is quite complicated. Briefly, however, terms  $b$  and  $c$  collectively describe how vibrational overlaps for a fully thermally equilibrated system depend on vibrational frequency, displacement, quantum number and temperature. Term  $d$  describes energy matching (energy conservation) effects, including solvent broadening effects. In the classical theory (eq. 4), term  $a$  is a component of the electronic prefactor. In the quantum treatment, however, it is better viewed as a component of the vibrational density of states parameter. Despite their complexity, eqs. 6 and 8 ultimately do yield results that are numerically identical to those from eq. 4 if all modes are made fully classical (i.e. all vibrational frequencies are made small with respect to  $kT$ ).

Figures 6 and 7 show the results of fully quantum mechanical  $k_{\text{ET}}$  versus overpotential calculations utilizing eqs. 6 and 8 plus sum-over-electronic-states corrections. The largest rate constants correspond in each case to “solvent only” barriers (where the calculations were implemented by using a high-frequency dummy mode in eq. 8, as previously described). The remaining rate plots correspond to calculations where individual vibrational modes are sequentially added, starting with the mode of lowest frequency. Tables 3 and 4 summarize these “mode specific” rate attenuation effects for reactivity under exchange conditions (zero driving force conditions). Note that for both

TCNE reduction and HMB oxidation, inclusion of multiple Franck-Condon-active vibrational modes exerts only modest effects upon the standard rate constant. (In contrast, much greater rate attenuation effects have been calculated for a related reaction, reduction of 4-cyano-N-methylpyridinium (4).)

Additional calculations were run where all modes were included, but individual modes were progressively made classical (by removing them from the explicitly vibrational part of eq. 8 and adding equivalent reorganization energy contributions to the corresponding solvent terms). These calculations offer some insight into the role of nuclear tunneling. Mode-specific tunneling effects were evaluated by taking ratios of rate constants calculated (eqs. 6 and 8) under quantum mechanical versus classical conditions. Again the results are summarized in Tables 3 and 4. As one might expect, the largest tunneling enhancement effects are associated with high frequency modes that are necessarily difficult to activate thermally. The *total* calculated tunneling enhancement effects for TCNE<sup>0/-</sup> and HMB<sup>+0</sup> are 2.2 and 1.4, respectively.

Finally, activation parameters at  $E = E_f$  were calculated by plotting  $\ln(k_{ET} \cdot T^{1/2})$  versus  $1/T$  for both classical and quantum mechanical reactions. From Table 5,  $\Delta H^*$ (classical) exceeds  $\Delta H^*$ (quantum) for both TCNE reduction and HMB oxidation. The differences are another manifestation of nuclear tunneling or, equivalently, barrier crossing without full thermal activation (see Figure 5). Classical activation entropies are zero, as expected, since redox-induced changes in vibrational frequencies have been neglected. Quantum mechanical activation entropies, on the other hand, are negative. Rather than reflecting true transition-state entropy effects, however, these parameters simply reflect the rather complex interplay in eq. 8 between Boltzmann effects, vibrational overlaps and overall reaction rates.

## CONCLUSIONS

Nominally "simple" outer-sphere electron transfer reactions can be complex in a vibrational reorganizational sense. For reactants capable of forming Mulliken-type charge transfer complexes, resonance Raman intensity data can be utilized to obtain unitless normal coordinate displacements, mode-specific vibrational reorganizational parameters and multi-dimensional potential energy surfaces for the corresponding electrochemical half reactions. The displacement and reorganizational parameters, in turn, can be employed in a multi-mode quantum rate formulation to obtain complete mode-specific descriptions of vibrational rate attenuation effects, driving force effects, temperature effects and nuclear tunneling effects.

## ACKNOWLEDGMENTS

We thank the Office of Naval Research, the DOD AAESERT program and the Dreyfus Foundation (Teacher-Scholar Award to JTH) for support of our work.

## REFERENCES

1. F. Markel, N. S. Ferris, I. R. Gould, A. B. Myers, *J. Am. Chem. Soc.* **114**, 6208(1992).
2. K. Kulinowski, I.R. Gould, N.S. Ferris, and A.B. Myers *J. Phys. Chem.* **99**, 17715 (1995)
3. J. L. Wooten, J. I. Zink, *J. Phys. Chem.*, **99**, 7251(1996).
4. D. C. Selmarten and J. T. Hupp, *Faraday Transactions*, submitted.
5. R. D. Williams, V. I. Petrov, H. P. Lu, J. T. Hupp, *Chem. Phys. Lett.* to be submitted.
6. D. I. Yoon, D. C. Selmarten, H-J. Liu, H. P. Lu, C. Mottley, M. A. Ratner, J. T. Hupp, *Chem. Phys. Lett.* **235**, 521(1995).
7. R. L. Blackbourn, C. S. Johnson and J. T. Hupp, *J. Am. Chem. Soc.* **113**, 1060(1991).
8. S. K. Doorn and J. T. Hupp, *J. Am. Chem. Soc.* **111**, 4704(1989).
9. S. K. Doorn and J. T. Hupp, *J. Am. Chem. Soc.* **111**, 1142(1989).
10. E. J. Heller, *Acc. Chem. Res.* **14**, 368(1981).
11. J. I. Zink, K-S. K. Shin, *Adv. Photochem.* **16**, 119(1991).
12. J. Jortner and M. Bixon, *J. Chem. Phys.* **88**, 167(1988).
13. D.L. Jeanmarie, M.R. Suchanski, and R.P. Van Duyne, *J. Am. Chem. Soc.* **97**, 1699 (1975)
14. F. Markel, N. S. Ferris, I.R. Gould, A.B. Myers, *J. Am. Chem. Soc.* **114**, 6208 (1992)
15. J. V. Caspar, T. D. Westmoreland, G. H. Allen, P. G. Bradley, T. J. Meyer and W. H. Woodruff, *J. Am. Chem. Soc.* **106**, 3492(1984).
16. R. M. Badger, *Phys. Rev.* **48**, 284(1935).
17. T.W. Cape, M.R. Suchanski, A.R. Siedle, R. P. Van Duyne, *J. Phys. Chem.* **90**, 739 (1986)
18. R. A. Marcus, *J. Chem. Phys.* **43**, 679(1965).
19. J. T. Hupp and M. J. Weaver, *J. Electroanal. Chem.* **152**, 1(1983).
20. G. E. McManis and M. J. Weaver, *Chem. Phys.* **48**, 452(1989).
21. W. R. Fawcett, *Angew. Chem., Int. Ed. Engl.* **34**, 194(1995).
22. H. Lu, J. N. Preiskorn and J. T. Hupp, *J. Am. Chem. Soc.* **115**, 4927(1993).
23. C. E. D. Chidsey, *Science*, **251**, 919(1991).
24. B. S. Brunschwig, N. Sutin, *Comm. Inorg. Chem.* **6**, 209(1987).
25. K. G. Spears, X. Wen and S. M. Arrivo, *J. Phys. Chem.*, **99**, 9693(1995).



Table I. Spectroscopic, Vibrational, and Structural Parameters for Tetracyanoethylene Reduction

Mode Frequency	$\Delta^a$	$\chi'_{\text{vib}}$	Assignment
2222 $\text{cm}^{-1}$	0.52	3.60 $\text{kJ mole}^{-1}$	$\longleftrightarrow$ $\text{C}\equiv\text{N}$
1551	1.04	10.0	$\longleftrightarrow$ $\text{C}=\text{C}$
600	0.64	1.50	$\longleftrightarrow$ $\text{C}-\text{C}$
542	0.61	1.20	$\text{C}-\text{C}\equiv\text{N}$ $\curvearrowright$

a. Derived from data in ref. 2, as described in text.

Table II. Spectroscopic, Vibrational, and Structural Parameters for Hexamethylbenzene Oxidation

Mode Frequency	$\Delta^a$	$\chi'_{\text{vib}}$	Assignment
1570 $\text{cm}^{-1}$	0.34	1.00 $\text{kJ mole}^{-1}$	ring str.
1437	0.27	0.63	$\text{CH}_3$ sym. def.
1386	0.35	0.24	?
1292	0.71	1.00	$\text{C}-\text{CH}_3$ str., ring str.
968	0.52	1.55	$\text{C}-\text{CH}_3$ str., ring def.
450	1.56	6.86	$\text{C}-\text{CH}_3$ def.

a. Derived from data in ref. 2, as described in text.

Table III: Mode-specific Rate Attenuation and Nuclear Tunneling Factors for TCNE Reduction


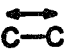


Mode	Rate Attenuation Factor	Nuclear Tunneling Factor	Assignment
542 cm <sup>-1</sup>	1.25	1.02	
600	1.15	1.03	
1551	1.69	1.80	
2222	1.14	1.03	

Table IV: Mode-specific Rate Attenuation and Nuclear Tunneling Factors for HMB Oxidation

Mode	Rate Attenuation Factor	Nuclear Tunneling Factor	Identity
450 cm <sup>-1</sup>	1.95	1.07	C-CH <sub>3</sub> def.
968	1.13	1.06	C-CH <sub>3</sub> str., ring def.
1292	1.23	1.22	C-CH <sub>3</sub> str., ring str.
1389	1.06	1.06	?
1437	1.04	1.04	CH <sub>3</sub> sym def.
1570	1.06	1.07	Ring str.

Table 5: Activation parameters for HMB oxidation and TCNE reduction.

	HMB	TCNE
$\Delta H^*$ (classical)	13 kJ mole <sup>-1</sup>	15 kJ mole <sup>-1</sup>
$\Delta H^*$ (quantum)	9 kJ mole <sup>-1</sup>	10 kJ mole <sup>-1</sup>
$\Delta S^*$ (classical)	0 J deg <sup>-1</sup> mole <sup>-1</sup>	0 J deg <sup>-1</sup> mole <sup>-1</sup>
$\Delta S^*$ (quantum)	-9 J deg <sup>-1</sup> mole <sup>-1</sup>	-10 J deg <sup>-1</sup> mole <sup>-1</sup>

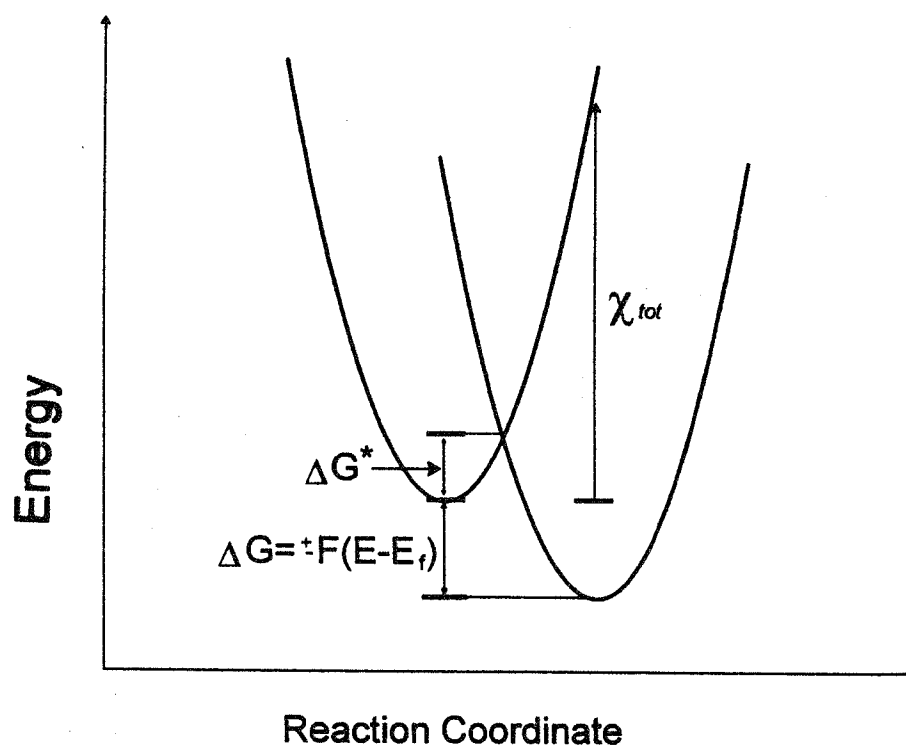
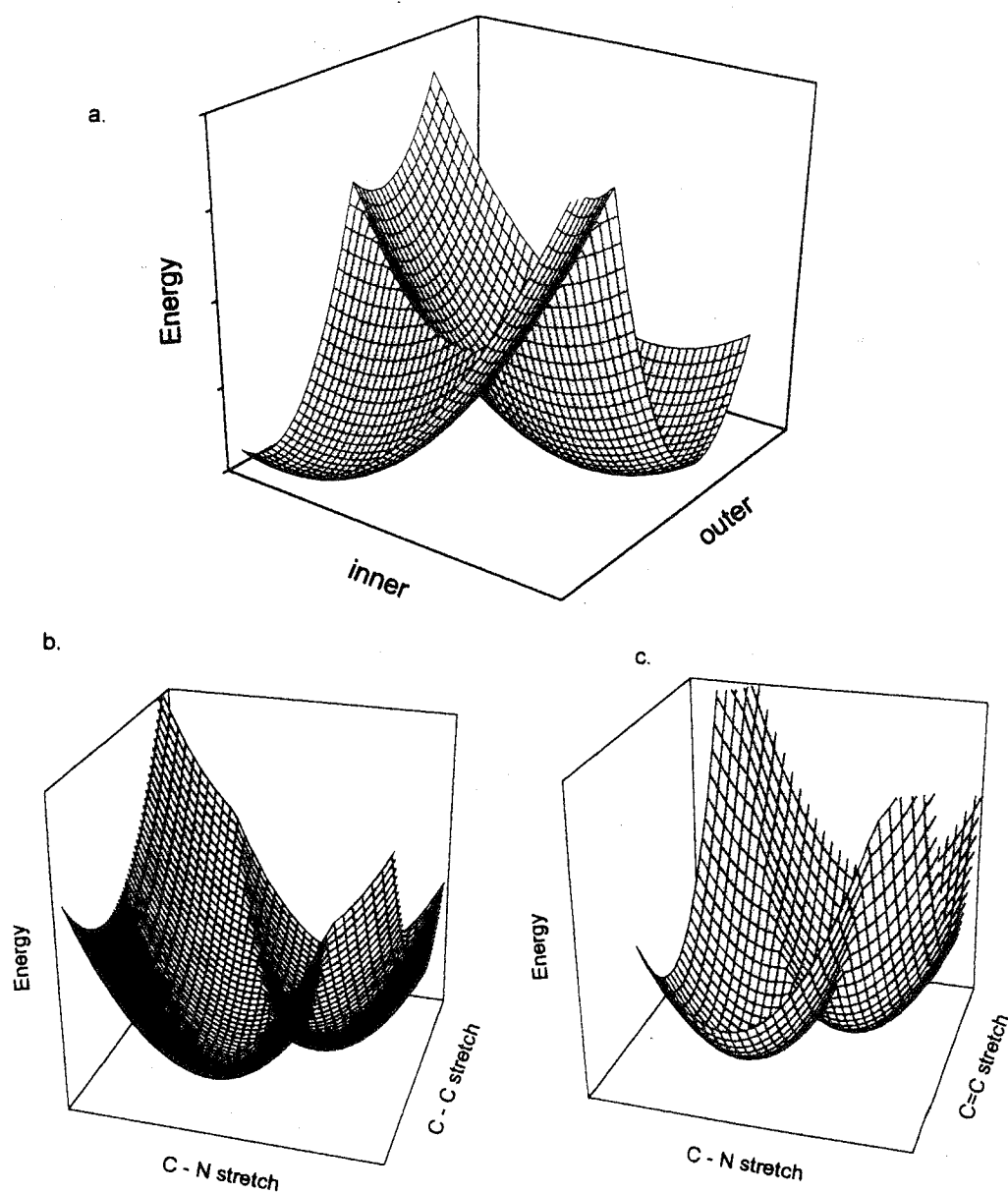


Figure 1. Simple potential energy surface showing driving force ( $\Delta G$ ), total reorganization energy ( $\chi_{tot}$ ), and the activation barrier ( $\Delta G^*$ ).



**Figure 2. Two dimensional potential energy surfaces for TCNE reduction: (a) solvent reorganization energy vs. vibrational reorganization energy, (b) C-N stretch vs. C-C stretch, (c) C-N stretch vs. C=C stretch.**

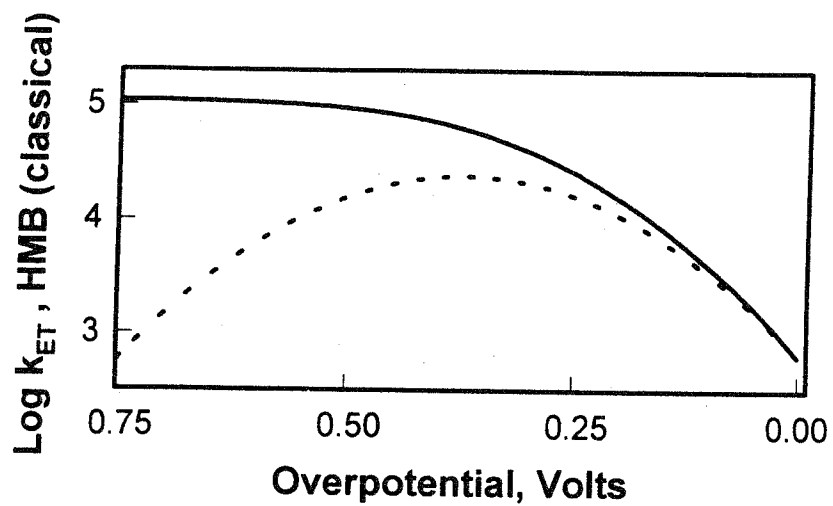


Figure 3. Dependence of calculated rate on overpotential for HMB oxidation, with (solid line) and without (dashed line) sum-over-electronic-states correction.

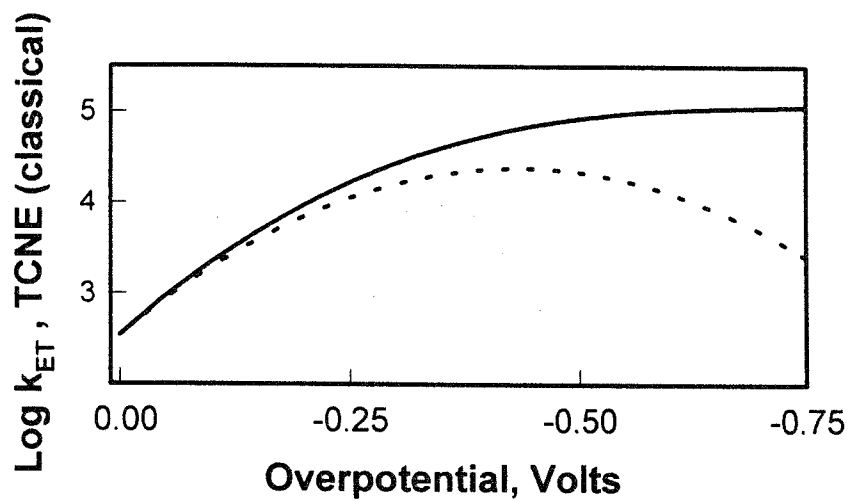


Figure 4. Dependence of calculated rate on overpotential for TCNE reduction, with (solid line) and without (dashed line) sum-over-electronic-states correction.

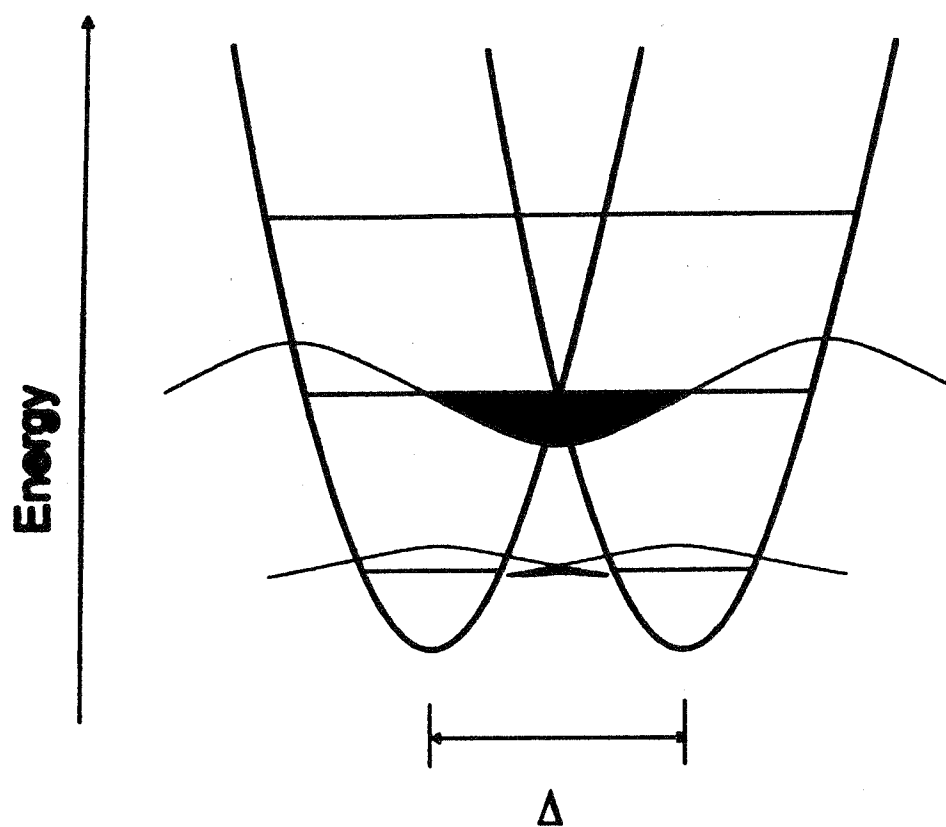


Figure 5. Potential energy surfaces for single mode quantum mechanical electron transfer reaction in the exchange limit. Shown are schematic representations of nuclear displacement, selected vibrational wavefunctions and vibrational wavefunction overlap.

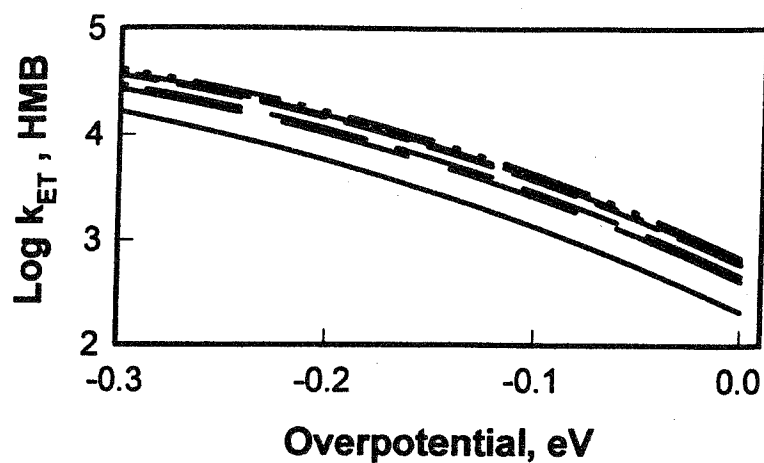


Figure 6. Results of quantum mechanical rate calculations for HMB oxidation: Top curve represents solvent only. Lower curves illustrate the effects of sequential vibrational mode addition (highest frequency to lowest frequency; note that some curves overlay).

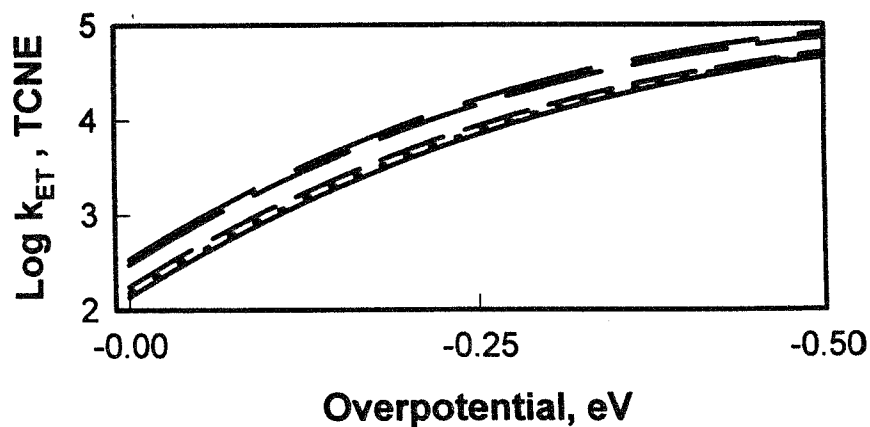


Figure 7. Results of quantum mechanical rate calculations for TCNE reduction: Top curve represents solvent only. Lower curves illustrate the effects of sequential vibrational mode addition (highest frequency to lowest frequency).